J. Plasma Phys. (2021), *vol*. 87, 905870406 © The Author(s), 2021.
Published by Cambridge University Press
doi:10.1017/S0022377821000702

Geometric electrostatic particle-in-cell algorithm on unstructured meshes

Zhenyu Wang [1],†, **Hong Qin** [1], **Benjamin Sturdevant** [1] **and C.S. Chang** [1]

[1]Princeton Plasma Physics Laboratory, Princeton University, Princeton, NJ 08543, USA

(Received 24 December 2020; revised 16 June 2021; accepted 21 June 2021)

We present a geometric particle-in-cell (PIC) algorithm on unstructured meshes for studying electrostatic perturbations with frequency lower than electron gyrofrequency in magnetized plasmas. In this method, ions are treated as fully kinetic particles and electrons are described by the adiabatic response. The PIC method is derived from a discrete variational principle on unstructured meshes. To preserve the geometric structure of the system, the discrete variational principle requires that the electric field is interpolated using Whitney 1-forms, the charge is deposited using Whitney 0-forms and the electric field is computed by discrete exterior calculus. The algorithm has been applied to study the ion Bernstein wave (IBW) in two-dimensional magnetized plasmas. The simulated dispersion relations of the IBW in a rectangular region agree well with theoretical results. In a two-dimensional circular region with fixed boundary condition, the spectrum and eigenmode structures of the IBW are obtained from simulations. We compare the energy conservation property of the geometric PIC algorithm derived from the discrete variational principle with that of previous PIC methods on unstructured meshes. The comparison shows that the new PIC algorithm significantly improves the energy conservation property.

Key words: plasma simulation, plasma waves

1. Introduction

Particle-in-cell (PIC) simulation is an important tool for plasma physics (Potter 1973; Dawson, Okuda & Rosen 1976; Hockney & Eastwood 1981; Dawson 1983; Birdsall & Langdon 1991). A structured mesh is easy to implement and widely used in PIC simulations. On the other hand, many studies require modelling of plasma in specific and complex geometries found in advanced tokamaks, stellarators, target chambers of inertial confinement fusion, etc., where unstructured meshes have a unique advantage. Electrostatic PIC schemes on unstructured meshes have been proposed (Celik *et al.* 2003; Spirkin & Gatsonis 2004; Gatsonis & Spirkin 2009; Day 2011; Han *et al.* 2016). In these schemes, the shape function for interpolating the electric field at particle positions is identical to that for depositing particle charge to the grid points of unstructured meshes. Numerical studies (Langdon 1970) showed that using the same shape function for charge deposition and field interpolation restricts the grid size to the Debye length. It is difficult to carry out large-scale simulations for collisionless plasma using these

† Email address for correspondence: zwang3@pppl.gov

electrostatic PIC schemes. In the previous PIC methods, the charge-deposition schemes and the field-interpolation schemes are independent. The shape functions for these two schemes can be chosen to be the same or different. There is no fundamental guiding principle on how to design the schemes. In the present study, we develop a geometric algorithm for electrostatic PIC simulations with adiabatic electrons on an unstructured mesh. Instead of selecting a shape function based on intuition or experience, we derive the charge-deposition and field-interpolation algorithm from an underpinning discrete variational principle.

Squire, Qin & Tang (2012*a*,*b*) first employed the methodology of discrete variational principle (Lee 1983; Veselov 1988; Marsden & West 2001; Qin & Guan 2008; Qin, Guan & Tang 2009; Qin 2020) to derive an electromagnetic PIC algorithm on an unstructured mesh. In that work, the technique of Whitney forms (Whitney 1957) was introduced for the first time to deposit charge and current and to interpolate fields. Discrete exterior calculus (Bossavit 1988, 1998; Hirani 2003) was also applied to compute the electromagnetic field on an unstructured mesh. It was demonstrated that the discrete variational principle admits the discrete electromagnetic gauge symmetry and thus ensures the discrete charge conservation (Squire *et al.* 2012*a*,*b*; Xiao *et al.* 2015*b*; Xiao, Qin & Liu 2018; Glasser & Qin 2020). Xiao *et al.* (2015*b*) developed an explicit high-order non-canonical symplectic electromagnetic PIC scheme starting from the discrete variational principles on a cubic mesh. High-order Whitney forms for cubic meshes were constructed and used for current deposition and electromagnetic field interpolation. It was found that the 'shape functions' for current deposition and field interpolation are different, and even for different components of the field the interpolation schemes are different. Similar and subsequent studies (Xiao *et al.* 2013, 2015*a*, 2017; Xiao & Qin 2019, 2021; Zheng *et al.* 2020) have also illustrated that discrete variational principles and Whitney forms are useful tools in designing structure-preserving geometric PIC algorithms (Squire *et al.* 2012*a*,*b*; He *et al.* 2015*a*; Xiao *et al.* 2015*b*; He *et al.* 2016*b*; Qin *et al.* 2016; Burby 2017; Kraus *et al.* 2017; Morrison 2017; Xiao *et al.* 2018; Li *et al.* 2019; Kormann & Sonnendrücker 2021; Perse, Kormann & Sonnendrücker 2021). Even for PIC algorithms that are not designed to preserve the geometric structures of the classical particle–field systems, the application of Whitney forms has been found to be beneficial (Moon, Teixeira & Omelchenko 2015).

In plasma physics, many reduced models are used, where comparing with the fully kinetic six-dimensional model, these reduced models keep certain physics of interest and simplify other less important dynamics. One widely adopted reduced model is the Vlasov–Poisson system with fully kinetic six-dimensional ions and adiabatic electrons, which is adequate for studying the low-frequency physics associated with ions. It is desirable to apply structure-preserving geometric algorithms to these models as well. A structure-preserving geometric PIC algorithm on a cubic mesh for this system was developed recently (Xiao & Qin 2019). The construction of the algorithm starts from a field theory, i.e. a variational principle. As in the geometric PIC algorithms for the Vlasov–Maxwell system, Whitney forms and variational symplectic integrators are employed. In particular, the charge-deposition and field-interpolation schemes were derived from the variational principle for the electrostatic dynamics in the cubic mesh.

We take a step-by-step approach to build a structure-preserving geometric PIC algorithm for the Vlasov–Poisson system on unstructured meshes. In the present work, we focus on the charge-deposition and field-interpolation methods and have not implemented the symplectic integrator. The Lagrangian of the system is discretized on an unstructured mesh, and the charge-deposition and field-interpolation methods are derived from the discrete variational principle on the unstructured mesh using Whitney forms. In place of a more structure-preserving symplectic integrator (He *et al.* 2015*a*, 2016*b*, 2017), the Boris

https://doi.org/10.1017/S0022377821000702 Published online by Cambridge University Press

algorithm (Boris 1970), which preserves the phase space volume (Qin *et al.* 2013; He *et al.* 2015*b*; Zhang *et al.* 2015; He *et al.* 2016*a*,*c*), is adopted to push particles. Our purpose here is to demonstrate how to design effective charge-deposition and field-interpolation algorithms on an unstructured mesh using the discrete field theory and Whitney forms. In addition, previous geometric PIC algorithms on unstructured meshes (Squire *et al.* 2012*a*,*b*; Moon *et al.* 2015) were built on simplicial meshes, i.e. triangular and tetrahedral meshes. In certain applications, it is advantageous to use partially unstructured meshes. For example, in the XGC code (Chang, Ku & Weitzner 2004; Ku *et al.* 2006, 2018; Chang *et al.* 2009, 2017), an unstructured triangular mesh is needed in the two-dimensional (2-D) poloidal plane and the grid in the toroidal direction is structured. In this work, we develop a geometric PIC algorithm on this type of unstructured prism mesh, starting from the discrete variational principle. To preserve geometric structure on the prism mesh, the discrete variational principle mandates that the Whitney 0-forms are used for charge deposition and the Whitney 1-forms for field interpolation. We self-consistently derive the Whitney 1-forms on the prism mesh from the discrete variational principle.

To validate the new PIC algorithm, we compare the dispersion relation of the ion Bernstein wave (IBW) from the PIC simulation with the theory (Sturdevant 2016; Sturdevant, Chen & Parker 2017) in a 2-D periodic plasma. Eigenmode structures of the IBW in a 2-D circular geometry with fixed boundary conditions are also simulated. We compare the simulation results with those of the conventional methods (Celik *et al.* 2003; Spirkin & Gatsonis 2004) on the same unstructured mesh, and find that our method is able to significantly reduce the energy error of the simulations.

The paper is organized as follows. In § 2, the geometric electrostatic PIC algorithm with fully kinetic ions and adiabatic electrons on an unstructured mesh is derived. Simulations of the IBW in an infinite 2-D geometry and a 2-D circular geometry are presented in § 3. We compare the energy conservation property of our algorithm with that of previous methods in § 4.

2. Geometric electrostatic PIC algorithm on an unstructured mesh

2.1. *Simplicial mesh*

In this subsection, we build the geometric electrostatic PIC algorithm on an unstructured simplicial mesh. The model treats ions as fully kinetic six-dimensional particles. The response of the electrons is adiabatic (Horton 1999; Weiland 2012; Sturdevant 2016; Hu *et al.* 2018; Miecnikowski *et al.* 2018), which, with the quasi-neutrality condition, leads to

$$-\frac{q_i}{q_e}n_i = n_{e0}\exp\left(-\frac{q_e\phi}{T_e}\right), \tag{2.1}$$

where n_i is the ion density, n_{e0} is the background electron density, ϕ is the electric potential, T_e is the electron temperature and q_e and q_i are electron and ion charges, respectively. The action integral of the system is (Xiao & Qin 2019)

$$S(\boldsymbol{x},\phi) = \int \mathrm{d}t L(\boldsymbol{x},\phi), \tag{2.2}$$

$$L = \int \mathrm{d}\boldsymbol{x}\,\mathrm{d}\boldsymbol{v} f_i(\boldsymbol{x},\boldsymbol{v})\left[\frac{1}{2}m_i\dot{\boldsymbol{x}}^2 + q_i\dot{\boldsymbol{x}}\cdot\boldsymbol{A}_0(\boldsymbol{x},t)\right]$$
$$-q_i[\phi(\boldsymbol{x},t)+\phi_0(\boldsymbol{x},t)] + n_{e0}T_e\exp\left[-\frac{q_e\phi(\boldsymbol{x},t)}{T_e}\right], \tag{2.3}$$

https://doi.org/10.1017/S0022377821000702 Published online by Cambridge University Press

where $\boldsymbol{x} = \boldsymbol{x}(\boldsymbol{x}_0, \boldsymbol{v}_0, t)$, f_i is the ion distribution function, m_i is ion mass and $\boldsymbol{A}_0$ and ϕ_0 are the external vector and scalar potentials. The dynamics of the system is governed by the Euler–Lagrange equations:

$$\frac{\delta S}{\delta \phi} = 0, \tag{2.4}$$

$$\frac{\delta S}{\delta \boldsymbol{x}} = 0. \tag{2.5}$$

Equation (2.4) links the electric potential ϕ and the ion charge density ρ_i:

$$\phi = -\frac{T_e}{q_e} \log\left(-\frac{\rho_i}{q_e n_{e0}}\right), \tag{2.6}$$

where $\rho_i = \int \mathrm{d}\boldsymbol{v} q_i f_i(\boldsymbol{x}, \boldsymbol{v})$. Equation (2.6) recovers the electron adiabatic response and charge-neutrality condition in (2.1). Equation (2.5) gives the equation of motion for particles:

$$\ddot{\boldsymbol{x}} = \frac{q_i}{m_i}[\boldsymbol{E}_0(\boldsymbol{x}, t) + \boldsymbol{E}(\boldsymbol{x}, t) + \dot{\boldsymbol{x}} \times \boldsymbol{B}_0(\boldsymbol{x}, t)], \tag{2.7}$$

where $\boldsymbol{E}_0(\boldsymbol{x}, t)$ and $\boldsymbol{B}_0(\boldsymbol{x}, t)$ are the external electromagnetic field, and $\boldsymbol{E}(\boldsymbol{x}, t) = -\nabla\phi(\boldsymbol{x}, t)$ is the perturbed electrostatic field.

We use the method introduced in Squire *et al.* (2012*a*) and Xiao & Qin (2019) to discretize the action integral by particles and Whitney forms (Whitney 1957) on a 2-D unstructured triangular mesh. The discrete action integral S_d can be written as

$$S_d(\boldsymbol{x}_p, \phi_I) = \int L_d(\boldsymbol{x}_p, \phi_I)\, \mathrm{d}t, \tag{2.8}$$

$$L_d(\boldsymbol{x}_p, \phi_I) = \sum_p \left[\frac{1}{2} m_i \dot{\boldsymbol{x}}_p^2 + q_i \dot{\boldsymbol{x}}_p \cdot \boldsymbol{A}_0(\boldsymbol{x}_p) - q_i \sum_I W_{\sigma_0, I}(\boldsymbol{x}_p)\phi_I - q_i \phi_0(\boldsymbol{x}_p)\right] + \sum_I n_{e0,I} T_{e,I} \exp\left(-\frac{q_e \phi_I}{T_{eI}}\right), \tag{2.9}$$

where I is the triangular vertex index, $\boldsymbol{x}_p$ is the particle position of the pth particle, ϕ_I is the electric potential defined on the triangular vertex and $W_{\sigma_0, I}$ is the Whitney 0-form interpolating the value of ϕ in continuous space using ϕ_I. The discrete action integral is the same as in Xiao & Qin (2019), except that here it is on a 2-D unstructured triangular mesh.

Variations of S_d with respect to ϕ_I and $\boldsymbol{x}_p$ lead to the equations of motion of the electrostatic system:

$$\frac{\delta S_d}{\delta \phi_I} = 0, \tag{2.10}$$

$$\frac{\delta S_d}{\delta \boldsymbol{x}_p} = 0. \tag{2.11}$$

Equation (2.10) gives

$$\phi_I = -\frac{T_{e,I}}{q_e} \log\left(-\frac{\rho_I}{q_e n_{e0,I}}\right), \tag{2.12}$$

https://doi.org/10.1017/S0022377821000702 Published online by Cambridge University Press

where

$$\rho_I = q_i W_{\sigma_0,I}(\boldsymbol{x}_p) \tag{2.13}$$

is the charge density on the triangular vertex. Equation (2.11) is the governing equation for ion dynamics:

$$\ddot{\boldsymbol{x}}_p = \frac{q_i}{m_i}\left[\boldsymbol{E}_0(\boldsymbol{x}_p, t) + \dot{\boldsymbol{x}}_p \times \boldsymbol{B}_0(\boldsymbol{x}_p, t) - \frac{\partial}{\partial \boldsymbol{x}_p}\sum_I W_{\sigma_0,I}(\boldsymbol{x}_p)\phi_I\right]. \tag{2.14}$$

The last term of (2.14) is the derivative of $W_{\sigma_0,I}$ with respect to $\boldsymbol{x}_p$ in continuous space. According to the property of Whitney forms (Whitney 1957; Hirani 2003; Desbrun, Kanso & Tong 2008; Squire *et al.* 2012*a*; Xiao *et al.* 2015*b*),

$$\nabla \sum_I W_{\sigma_0,I}(\boldsymbol{x}_p)\phi_I = \sum_J W_{\sigma_1,J}(\boldsymbol{x}_p)\sum_I \nabla_{dJ,I}\phi_I, \tag{2.15}$$

where $\sum_I \nabla_{dJ,I}\phi_I$ is the discrete gradient of ϕ_I, and $W_{\sigma_1,J}$ is the Whitney 1-form that interpolates a continuous 1-form from the discrete 1-form defined on the triangular edge. The construction of $W_{\sigma_0,I}$, $W_{\sigma_1,J}$ and $\nabla_{dJ,I}$ is further discussed below. With property (2.15), (2.14) becomes

$$\ddot{\boldsymbol{x}}_p = \frac{q_i}{m_i}\left[\boldsymbol{E}_0(\boldsymbol{x}_p, t) + \dot{\boldsymbol{x}}_p \times \boldsymbol{B}_0(\boldsymbol{x}_p, t) + \sum_J W_{\sigma_1,J}(\boldsymbol{x}_p)\boldsymbol{E}_J\right] \tag{2.16}$$

and

$$\boldsymbol{E}_J = -\sum_I \nabla_{dJ,I}\phi_I, \tag{2.17}$$

where $\boldsymbol{E}_J$ is the discrete electrical field defined on the triangular edge labelled by J. We want to emphasize again that, similar to the scenario in a cubic mesh (Xiao & Qin 2019), without Whitney forms and discrete exterior calculus, it is difficult to calculate on the electric field on an unstructured mesh to advance particle positions.

As is well known, the key parts of a PIC method include charge deposition, solving discrete field and field interpolation, which are encapsulated in a systematic way in (2.13), (2.17) and (2.16), respectively. Once $W_{\sigma_0,I}$, $W_{\sigma_1,J}$ and $\nabla_{dJ,I}$ are chosen, the PIC algorithm is defined.

Now we describe in detail the construction of $W_{\sigma_0,I}$, $W_{\sigma_1,J}$ and $\nabla_{dJ,I}$ on the triangular mesh. Figure 1(*a*) shows a particle in a triangle, where (x, y) is the position of the particle p, and the three vertices of the ith triangle, i_1, i_2, i_3, have coordinates (x_{i_1}, y_{i_1}), (x_{i_2}, y_{i_2}), (x_{i_3}, y_{i_3}), respectively. To deposit charge at each vertex according to (2.13), we need to specify the Whitney 0-forms, which are chosen to be linear barycentric functions. For (x, y) inside the triangle, the Whitney 0-forms are

$$W_{\sigma_0,i_1}(x, y) = \frac{(y_{i_2} - y_{i_3})(x - x_{i_3}) + (x_{i_3} - x_{i_2})(y - y_{i_3})}{(x_{i_1} - x_{i_3})(y_{i_2} - y_{i_3}) + (x_{i_3} - x_{i_2})(y_{i_1} - y_{i_3})}, \tag{2.18}$$

$$W_{\sigma_0,i_2}(x, y) = \frac{(y_{i_3} - y_{i_1})(x - x_{i_3}) + (x_{i_1} - x_{i_3})(y - y_{i_3})}{(x_{i_1} - x_{i_3})(y_{i_2} - y_{i_3}) + (x_{i_3} - x_{i_2})(y_{i_1} - y_{i_3})}, \tag{2.19}$$

$$W_{\sigma_0,i_3}(x, y) = 1 - W_{\sigma_0,i_1}(x, y) - W_{\sigma_0,i_2}(x, y). \tag{2.20}$$

When (x, y) is outside the triangle, all the Whitney 0-forms vanish. Note that $W_{\sigma_0,i_1}(x, y)$, $W_{\sigma_0,i_2}(x, y)$ and $W_{\sigma_0,i_3}(x, y)$ are the areas of the triangle $\Delta p i_2 i_3$, $\Delta p i_3 i_1$ and

https://doi.org/10.1017/S0022377821000702 Published online by Cambridge University Press

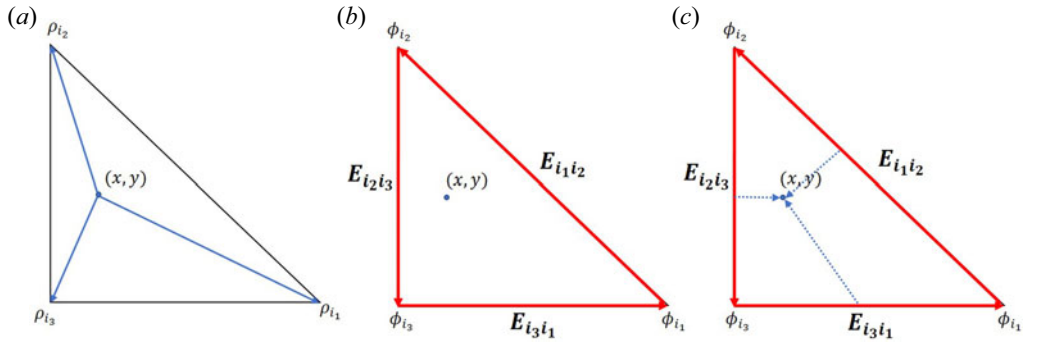

FIGURE 1. The PIC algorithm on a triangle. (*a*) Depositing a particle's charge to the triangular vertices using Whitney 0-forms $W_{\sigma_0,I}$. (*b*) Computing $\boldsymbol{E}_J$ on the edge with the discrete gradient operator $\nabla_{dJ,I}$. (*c*) Interpolating $\boldsymbol{E}_J$ from edges to the particle's location through Whitney 1-forms $W_{\sigma_1,J}$.

Δpi_1i_2, respectively. Thus, the weighting of charge deposition with respect to a vertex is the area weighting of the triangle enclosed by the particle and the opposite edge of the vertex. The density plots of $W_{\sigma_0,i_1}(x, y)$, $W_{\sigma_0,i_2}(x, y)$ and $W_{\sigma_0,i_3}(x, y)$ are shown in figure 2(*a–c*). Figure 2(*a*) shows $W_{\sigma_0,i_1}(x, y)$ approaching 1 as the particle is close to the vertex i_1. The chosen Whitney 0-forms in (2.18)–(2.20) obviously satisfy the condition

$$\sum_{I=i_1,i_2,i_3} W_{\sigma_0,I}(\boldsymbol{x}_p) = 1. \tag{2.21}$$

In the 2-D triangular mesh, 1-forms, such as $\boldsymbol{E}_J$, are defined on the triangular edges. And the index J for the edges consists of an ordered pair of indices of the vertices. For example, $J = i_1i_2$ labels the oriented edge from i_1 to i_2, as shown in figure 1(*b*). The discrete gradient operator $\nabla_{dJ,I}$ consistent with (2.15) is

$$\nabla_{di_1i_2,I} = \delta_{i_2I} - \delta_{i_1I}. \tag{2.22}$$

According to the definition of Whitney forms (Whitney 1957), the Whitney 1-form on an unstructured triangular mesh is

$$W_{\sigma_1,j'j} = W_{\sigma_0,j}\nabla W_{\sigma_0,j'} - W_{\sigma_0,j'}\nabla W_{\sigma_0,j}. \tag{2.23}$$

For the triangular mesh, the expressions of $W_{\sigma_1,j'j}(x, y)$ for $j', j = i_1, i_2, i_3$ and $j' \neq j$ are

$$W_{\sigma_1,i_1i_2}(x, y) = \left[\frac{(y_{i_3} - y_{i_1})W_{\sigma_0,i_1}(x, y) - (y_{i_2} - y_{i_3})W_{\sigma_0,i_2}(x, y)}{(x_{i_1} - x_{i_3})(y_{i_2} - y_{i_3}) + (x_{i_3} - x_{i_2})(y_{i_1} - y_{i_3})}, \right.$$
$$\left. \frac{(x_{i_1} - x_{i_3})W_{\sigma_0,i_1}(x, y) - (x_{i_3} - x_{i_2})W_{\sigma_0,i_2}(x, y)}{(x_{i_1} - x_{i_3})(y_{i_2} - y_{i_3}) + (x_{i_3} - x_{i_2})(y_{i_1} - y_{i_3})}\right], \tag{2.24}$$

$$W_{\sigma_1,i_2i_3}(x, y) = \left[\frac{(y_{i_1} - y_{i_2})W_{\sigma_0,i_2}(x, y) - (y_{i_3} - y_{i_1})W_{\sigma_0,i_3}(x, y)}{(x_{i_1} - x_{i_3})(y_{i_2} - y_{i_3}) + (x_{i_3} - x_{i_2})(y_{i_1} - y_{i_3})}, \right.$$
$$\left. \frac{(x_{i_2} - x_{i_1})W_{\sigma_0,i_2}(x, y) - (x_{i_1} - x_{i_3})W_{\sigma_0,i_3}(x, y)}{(x_{i_1} - x_{i_3})(y_{i_2} - y_{i_3}) + (x_{i_3} - x_{i_2})(y_{i_1} - y_{i_3})}\right], \tag{2.25}$$

https://doi.org/10.1017/S0022377821000702 Published online by Cambridge University Press

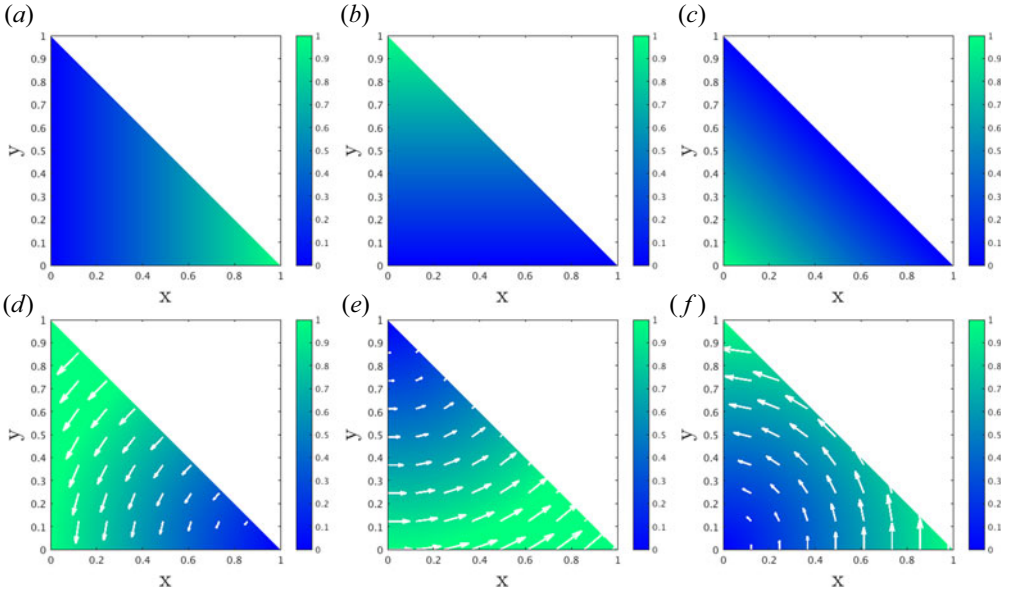

FIGURE 2. The values of the Whitney 0-forms and 1-forms. The density plot of the value of (*a*) $W_{\sigma_0,i_1}(x,y)$, (*b*) $W_{\sigma_0,i_2}(x,y)$ and (*c*) $W_{\sigma_0,i_3}(x,y)$. The amplitude density plot and the quiver plot of (*d*) $W_{\sigma_1,i_2i_3}(x,y)$, (*e*) $W_{\sigma_1,i_3i_1}(x,y)$ and (*f*) $W_{\sigma_1,i_1i_2}(x,y)$.

$$W_{\sigma_1,i_3i_1}(x,y) = \left[\frac{(y_{i_2}-y_{i_3})W_{\sigma_0,i_3}(x,y) - (y_{i_1}-y_{i_2})W_{\sigma_0,i_1}(x,y)}{(x_{i_1}-x_{i_3})(y_{i_2}-y_{i_3}) + (x_{i_3}-x_{i_2})(y_{i_1}-y_{i_3})}, \right.$$
$$\left. \frac{(x_{i_3}-x_{i_2})W_{\sigma_0,i_3}(x,y) - (x_{i_2}-x_{i_1})W_{\sigma_0,i_1}(x,y)}{(x_{i_1}-x_{i_3})(y_{i_2}-y_{i_3}) + (x_{i_3}-x_{i_2})(y_{i_1}-y_{i_3})}\right], \tag{2.26}$$

for (x,y) inside the triangle. All $W_{\sigma_1,j'j}(x,y)$ vanish when (x,y) is outside the triangle. The amplitude density plot and the quiver plot of $W_{\sigma_1,i_2i_3}(x,y)$ are shown in figure 2(*d*), where the amplitude approaches zero when a particle is close to the opposite vertex of the edge and maximizes when the particle approaches the edge. Figures 2(*e*) and 2(*f*) plot the value and direction of $W_{\sigma_1,i_3i_1}(x,y)$ and $W_{\sigma_1,i_1i_2}(x,y)$.

After $W_{\sigma_0,I}$, $W_{\sigma_1,J}$ and $\nabla_{dJ,I}$ are chosen, the discrete electric potential ϕ_I at each vertex can be calculated by (2.13) and (2.12), and the electric field on the edges according to (2.17) is

$$E_{i_1i_2} = \phi_{i_2} - \phi_{i_1}, \tag{2.27}$$

where $E_{i_1i_2}$ is a discrete 1-form, denoted by a boldface symbol in figure 1 following the convention of physicists. Particles' positions and velocities are advanced according to (2.16), which interpolates the electrical field at $\boldsymbol{x}_p$ as $\boldsymbol{E}(\boldsymbol{x}_p) = \sum_J W_{\sigma_1,J}(\boldsymbol{x}_p)\boldsymbol{E}_J$ using Whitney 1-forms. This process is illustrated in figure 1(*c*). In the current implementation, (2.16) is integrated by the Boris algorithm (Boris 1970), which preserves the phase space volume (Qin *et al.* 2013; Ellison, Burby & Qin 2015; He *et al.* 2015*b*, 2016*a*; Zhang *et al.* 2015; He *et al.* 2016*c*) although is not symplectic. The algorithm on a three-dimensional tetrahedral mesh can also be constructed in the same way.

https://doi.org/10.1017/S0022377821000702 Published online by Cambridge University Press

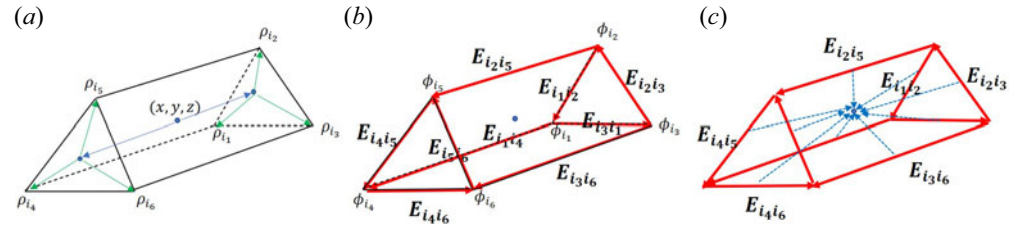

FIGURE 3. The PIC algorithm on prism mesh. (*a*) Charge-deposition algorithm. Here $\rho_{i_1}, \ldots, \rho_{i_6}$ are the charge density on the vertices deposited from a particle at (x, y, z). (*b*) Potentials $\phi_{i_1}, \ldots, \phi_{i_6}$ are electric potentials on the vertices, and $\boldsymbol{E}_{i_2i_3}, \boldsymbol{E}_{i_3i_1}, \boldsymbol{E}_{i_4i_5}, \boldsymbol{E}_{i_5i_6}, \boldsymbol{E}_{i_6i_4}, \boldsymbol{E}_{i_1i_4}, \boldsymbol{E}_{i_2i_5}, \boldsymbol{E}_{i_3i_6}$ are discrete electric field on the edges. (*c*) Field-interpolation algorithm. Note that $\boldsymbol{E}_{i_3i_1}$, $\boldsymbol{E}_{i_5i_6}$ and $\boldsymbol{E}_{i_1i_4}$ are not labelled for clarity.

2.2. *Three-dimensional non-simplicial mesh*

In this subsection, we develop the algorithm in a special non-simplicial mesh made of prisms. The mesh is constructed from a 2-D unstructured simplicial mesh and a structured grid in the third perpendicular dimension. This type of unstructured mesh has been adopted by the XGC code (Chang *et al.* 2004, 2009, 2017; Ku *et al.* 2006, 2018), where the structured direction is the toroidal direction, and the poloidal plane is covered by a 2-D unstructured simplicial mesh. The discrete variational principle, (2.4), gives the electric potential on a prism:

$$\phi_I = -\frac{T_{e,I}}{q_e} \log\left(-\frac{\rho_I}{q_e n_{e0,I}}\right), \tag{2.28}$$

where

$$\rho_I = q_i f_I(\boldsymbol{x}_p). \tag{2.29}$$

Equation (2.29) describes charge deposition on a prism with the function f_I defined as

$$\sum_{I=i_1,\ldots,i_6} f_I(\boldsymbol{x}_p) = f_{i_1}(\boldsymbol{x}_p) + f_{i_2}(\boldsymbol{x}_p) + f_{i_3}(\boldsymbol{x}_p) + f_{i_4}(\boldsymbol{x}_p) + f_{i_5}(\boldsymbol{x}_p) + f_{i_6}(\boldsymbol{x}_p), \tag{2.30}$$

where $i_1, \ldots, i_6$ label vertices 1 to 6 of the ith prism. Define $f_{i_1}(\boldsymbol{x}_p) = f_{\Delta_1,i_1}(x, y) f_{\Delta_1}(z)$, where Δ_1 is the back triangle of the prism, (x, y) is the position of the particle in the plane containing the triangle, $f_{\Delta_1,i_1}(x, y)$ gives the weighting of (x, y) with respect to i_1 on the triangle Δ_1 and z is the particle's position along the direction perpendicular to the triangle plane. Similarly, we define $f_{i_4}(\boldsymbol{x}_p) = f_{\Delta_2,i_4}(x, y) f_{\Delta_2}(z)$, where Δ_2 is the front triangle of the prism. Functions $f_{i_2}(\boldsymbol{x}_p), f_{i_3}(\boldsymbol{x}_p), f_{i_5}(\boldsymbol{x}_p)$ and $f_{i_6}(\boldsymbol{x}_p)$ are defined in a similar way (see figure 3*a*). Since Δ_1 and Δ_2 are identical, the weightings of (x, y) with respect to the corresponding vertices i_1 and i_4 are identical, i.e.

$$f_{\Delta_1,i_1}(x, y) = f_{\Delta_2,i_4}(x, y), \tag{2.31}$$

and

$$f_{\Delta_1,i_2}(x, y) = f_{\Delta_2,i_5}(x, y), \tag{2.32}$$

$$f_{\Delta_1,i_3}(x, y) = f_{\Delta_2,i_6}(x, y). \tag{2.33}$$

https://doi.org/10.1017/S0022377821000702 Published online by Cambridge University Press

Hence, (2.30) can be written as

$$\begin{aligned} & f_{i_1}(\boldsymbol{x}_p)+f_{i_2}(\boldsymbol{x}_p)+f_{i_3}(\boldsymbol{x}_p)+f_{i_4}(\boldsymbol{x}_p)+f_{i_5}(\boldsymbol{x}_p)+f_{i_6}(\boldsymbol{x}_p) \\ &\quad = [f_{\Delta_1,i_1}(x,y)+f_{\Delta_1,i_2}(x,y)+f_{\Delta_1,i_3}(x,y)]f_{\Delta_1}(z) \\ &\qquad + [f_{\Delta_2,i_4}(x,y)+f_{\Delta_2,i_5}(x,y)+f_{\Delta_2,i_6}(x,y)]f_{\Delta_2}(z) \\ &\quad = [f_{\Delta_1,i_1}(x,y)+f_{\Delta_1,i_2}(x,y)+f_{\Delta_1,i_3}(x,y)](f_{\Delta_1}(z)+f_{\Delta_2}(z)). \end{aligned} \tag{2.34}$$

By choosing $f_{\Delta_1,i_1}(x,y)+f_{\Delta_1,i_2}(x,y)+f_{\Delta_1,i_3}(x,y)=1$ and $f_{\Delta_1}(z)+f_{\Delta_2}(z)=1$, we have $\sum_{I-i_1,\ldots,i_6} f(\boldsymbol{x}_p)=1$. Equation (2.11) gives the governing equation for ion dynamics:

$$\ddot{\boldsymbol{x}}_p = \frac{q_i}{m_i}\left[\boldsymbol{E}_0(\boldsymbol{x}_p,t)+\dot{\boldsymbol{x}}_p\times\boldsymbol{B}_0(\boldsymbol{x}_p,t)-\frac{\partial}{\partial \boldsymbol{x}_p}\sum_I f_I(\boldsymbol{x}_p)\phi_I\right]. \tag{2.35}$$

The last term of (2.35) is

$$-\frac{\partial}{\partial \boldsymbol{x}_p}\sum_{I=i_1,\ldots,i_6} f_I(\boldsymbol{x}_p)\phi_I = -\phi_{i_1}\nabla f_{i_1}-\phi_{i_2}\nabla f_{i_2}-\phi_{i_3}\nabla f_{i_3}-\phi_{i_4}\nabla f_{i_4}-\phi_{i_5}\nabla f_{i_5}-\phi_{i_6}\nabla f_{i_6}, \tag{2.36}$$

which can be further expressed as

$$\begin{aligned} & -\phi_{i_1}\nabla f_{i_1}-\phi_{i_2}\nabla f_{i_2}-\phi_{i_3}\nabla f_{i_3}-\phi_{i_4}\nabla f_{i_4}-\phi_{i_5}\nabla f_{i_5}-\phi_{i_6}\nabla f_{i_6} \\ &\quad = f_{\Delta_1}(z)[-\phi_{i_1}\nabla_\perp f_{\Delta_1,i_1}(x,y)-\phi_{i_2}\nabla_\perp f_{\Delta_1,i_2}(x,y)-\phi_{i_3}\nabla_\perp f_{\Delta_1,i_3}(x,y)] \\ &\qquad + f_{\Delta_2}(z)[-\phi_{i_4}\nabla_\perp f_{\Delta_2,i_4}(x,y)-\phi_{i_5}\nabla_\perp f_{\Delta_2,i_5}(x,y)-\phi_{i_6}\nabla_\perp f_{\Delta_2,i_6}(x,y)] \\ &\qquad - \phi_{i_1} f_{\Delta_1,i_1}(x,y)\frac{\partial}{\partial z}f_{\Delta_1}(z)-\phi_{i_4} f_{\Delta_2,i_4}(x,y)\frac{\partial}{\partial z}f_{\Delta_2}(z) \\ &\qquad - \phi_{i_2} f_{\Delta_1,i_2}(x,y)\frac{\partial}{\partial z}f_{\Delta_1}(z)-\phi_{i_5} f_{\Delta_2,i_5}(x,y)\frac{\partial}{\partial z}f_{\Delta_2}(z) \\ &\qquad - \phi_{i_3} f_{\Delta_1,i_3}(x,y)\frac{\partial}{\partial z}f_{\Delta_1}(z)-\phi_{i_6} f_{\Delta_2,i_6}(x,y)\frac{\partial}{\partial z}f_{\Delta_2}(z), \end{aligned} \tag{2.37}$$

where $\nabla_\perp = (\partial/\partial x+\partial/\partial y)$. The first term of the right-hand side of (2.37) can be expressed as

$$\begin{aligned} & f_{\Delta_1}(z)[-\phi_{i_1}\nabla_\perp f_{\Delta_1,i_1}(x,y)-\phi_{i_2}\nabla_\perp f_{\Delta_1,i_2}(x,y)-\phi_{i_3}\nabla_\perp f_{\Delta_1,i_3}(x,y)] \\ &\quad = f_{\Delta_1}(z)[(\phi_{i_2}-\phi_{i_1})(f_{\Delta_1,i_2}(x,y)\nabla_\perp f_{\Delta_1,i_1}(x,y)-f_{\Delta_1,i_1}(x,y)\nabla_\perp f_{\Delta_1,i_2}(x,y)) \\ &\qquad + (\phi_{i_3}-\phi_{i_2})(f_{\Delta_1,i_3}(x,y)\nabla_\perp f_{\Delta_1,i_2}(x,y)-f_{\Delta_1,i_2}(x,y)\nabla_\perp f_{\Delta_1,i_3}(x,y)) \\ &\qquad + (\phi_{i_1}-\phi_{i_3})(f_{\Delta_1,i_1}(x,y)\nabla_\perp f_{\Delta_1,i_3}(x,y)-f_{\Delta_1,i_3}(x,y)\nabla_\perp f_{\Delta_1,i_1}(x,y))]. \end{aligned} \tag{2.38}$$

Similarly, the second term of the right-hand side of (2.37) is

$$\begin{aligned} & f_{\Delta_2}(z)[-\phi_{i_4}\nabla_\perp f_{\Delta_2,i_4}(x,y)-\phi_{i_5}\nabla_\perp f_{\Delta_2,i_5}(x,y)-\phi_{i_6}\nabla_\perp f_{\Delta_2,i_6}(x,y)] \\ &\quad = f_{\Delta_2}(z)[(\phi_{i_5}-\phi_{i_4})(f_{\Delta_2,i_5}(x,y)\nabla_\perp f_{\Delta_2,i_4}(x,y)-f_{\Delta_2,i_4}(x,y)\nabla_\perp f_{\Delta_2,i_5}(x,y)) \\ &\qquad + (\phi_{i_6}-\phi_{i_5})(f_{\Delta_2,i_6}(x,y)\nabla_\perp f_{\Delta_2,i_5}(x,y)-f_{\Delta_2,i_5}(x,y)\nabla_\perp f_{\Delta_2,i_6}(x,y)) \\ &\qquad + (\phi_{i_4}-\phi_{i_6})(f_{\Delta_2,i_4}(x,y)\nabla_\perp f_{\Delta_2,i_6}(x,y)-f_{\Delta_2,i_6}(x,y)\nabla_\perp f_{\Delta_2,i_4}(x,y))]. \end{aligned} \tag{2.39}$$

https://doi.org/10.1017/S0022377821000702 Published online by Cambridge University Press

Based on (2.31), the third term of (2.37) can be written as

$$\begin{aligned}
&-\phi_{i_1} f_{\Delta_1,i_1}(x,y)\frac{\partial}{\partial z}f_{\Delta_1}(z) - \phi_{i_4} f_{\Delta_2,i_4}(x,y)\frac{\partial}{\partial z}f_{\Delta_2}(z)\\
&\quad = f_{\Delta_1,i_1}(x,y)\left[-\phi_{i_1}\frac{\partial}{\partial z}f_{\Delta_1}(z) - \phi_{i_4}\frac{\partial}{\partial z}f_{\Delta_2}(z)\right]\\
&\quad = (\phi_{i_4}-\phi_{i_1}) f_{\Delta_1,i_1}(x,y)\left[f_{\Delta_2}(z)\frac{\partial}{\partial z}f_{\Delta_1}(z) - f_{\Delta_1}(z)\frac{\partial}{\partial z}f_{\Delta_2}(z)\right]. \qquad (2.40)
\end{aligned}$$

Similarly, the last two terms of (2.37) can be written as

$$\begin{aligned}
&-\phi_{i_2} f_{\Delta_1,i_2}(x,y)\frac{\partial}{\partial z}f_{\Delta_1}(z) - \phi_{i_5} f_{\Delta_2,i_5}(x,y)\frac{\partial}{\partial z}f_{\Delta_2}(z)\\
&\quad = (\phi_{i_5}-\phi_{i_2}) f_{\Delta_1,i_2}(x,y)\left[f_{\Delta_2}(z)\frac{\partial}{\partial z}f_{\Delta_1}(z) - f_{\Delta_1}(z)\frac{\partial}{\partial z}f_{\Delta_2}(z)\right] \qquad (2.41)
\end{aligned}$$

and

$$\begin{aligned}
&-\phi_{i_3} f_{\Delta_1,i_3}(x,y)\frac{\partial}{\partial z}f_{\Delta_1}(z) - \phi_{i_6} f_{\Delta_2,i_6}(x,y)\frac{\partial}{\partial z}f_{\Delta_2}(z)\\
&\quad = (\phi_{i_6}-\phi_{i_3}) f_{\Delta_1,i_3}(x,y)\left[f_{\Delta_2}(z)\frac{\partial}{\partial z}f_{\Delta_1}(z) - f_{\Delta_1}(z)\frac{\partial}{\partial z}f_{\Delta_2}(z)\right]. \qquad (2.42)
\end{aligned}$$

Finally, (2.36) is written as

$$\begin{aligned}
&-\phi_{i_1}\nabla f_{i_1} - \phi_{i_2}\nabla f_{i_2} - \phi_{i_3}\nabla f_{i_3} - \phi_{i_4}\nabla f_{i_4} - \phi_{i_5}\nabla f_{i_5} - \phi_{i_6}\nabla f_{i_6}\\
&= f_{\Delta_1}(z)[(\phi_{i_2}-\phi_{i_1})(f_{\Delta_1,i_2}(x,y)\nabla_\perp f_{\Delta_1,i_1}(x,y) - f_{\Delta_1,i_1}(x,y)\nabla_\perp f_{\Delta_1,i_2}(x,y))\\
&\quad + (\phi_{i_3}-\phi_{i_2})(f_{\Delta_1,i_3}(x,y)\nabla_\perp f_{\Delta_1,i_2}(x,y) - f_{\Delta_1,i_2}(x,y)\nabla_\perp f_{\Delta_1,i_3}(x,y))\\
&\quad + (\phi_{i_1}-\phi_{i_3})(f_{\Delta_1,i_1}(x,y)\nabla_\perp f_{\Delta_1,i_3}(x,y) - f_{\Delta_1,i_3}(x,y)\nabla_\perp f_{\Delta_1,i_1}(x,y))]\\
&\quad + f_{\Delta_2}(z)[(\phi_{i_5}-\phi_{i_4})(f_{\Delta_2,i_5}(x,y)\nabla_\perp f_{\Delta_2,i_4}(x,y) - f_{\Delta_2,i_4}(x,y)\nabla_\perp f_{\Delta_2,i_5}(x,y))\\
&\quad + (\phi_{i_6}-\phi_{i_5})(f_{\Delta_2,i_6}(x,y)\nabla_\perp f_{\Delta_2,i_5}(x,y) - f_{\Delta_2,i_5}(x,y)\nabla_\perp f_{\Delta_2,i_6}(x,y))\\
&\quad + (\phi_{i_4}-\phi_{i_6})(f_{\Delta_2,i_4}(x,y)\nabla_\perp f_{\Delta_2,i_6}(x,y) - f_{\Delta_2,i_6}(x,y)\nabla_\perp f_{\Delta_2,i_4}(x,y))]\\
&\quad + (\phi_{i_4}-\phi_{i_1}) f_{\Delta_1,i_1}(x,y)\left[f_{\Delta_2}(z)\frac{\partial}{\partial z}f_{\Delta_1}(z) - f_{\Delta_1}(z)\frac{\partial}{\partial z}f_{\Delta_2}(z)\right]\\
&\quad + (\phi_{i_5}-\phi_{i_2}) f_{\Delta_1,i_2}(x,y)\left[f_{\Delta_2}(z)\frac{\partial}{\partial z}f_{\Delta_1}(z) - f_{\Delta_1}(z)\frac{\partial}{\partial z}f_{\Delta_2}(z)\right]\\
&\quad + (\phi_{i_6}-\phi_{i_3}) f_{\Delta_1,i_3}(x,y)\left[f_{\Delta_2}(z)\frac{\partial}{\partial z}f_{\Delta_1}(z) - f_{\Delta_1}(z)\frac{\partial}{\partial z}f_{\Delta_2}(z)\right]. \qquad (2.43)
\end{aligned}$$

Inserting (2.43) into (2.35), the equation of motion for particles on the prism mesh is

$$\begin{aligned}
\ddot{\boldsymbol{x}}_p = \frac{q_i}{m_i}[&\boldsymbol{E}_0(\boldsymbol{x}_p,t) + \dot{\boldsymbol{x}}_p \times \boldsymbol{B}_0(\boldsymbol{x}_p,t)\\
&+ g_{i_1i_2}(\boldsymbol{x}_p)\boldsymbol{E}_{i_1i_2} + g_{i_2i_3}(\boldsymbol{x}_p)\boldsymbol{E}_{i_2i_3} + g_{i_3i_1}(\boldsymbol{x}_p)\boldsymbol{E}_{i_3i_1}\\
&+ g_{i_4i_5}(\boldsymbol{x}_p)\boldsymbol{E}_{i_4i_5} + g_{i_5i_6}(\boldsymbol{x}_p)\boldsymbol{E}_{i_5i_6} + g_{i_6i_4}(\boldsymbol{x}_p)\boldsymbol{E}_{i_6i_4}\\
&+ g_{i_1i_4}(\boldsymbol{x}_p)\boldsymbol{E}_{i_1i_4} + g_{i_2i_5}(\boldsymbol{x}_p)\boldsymbol{E}_{i_2i_5} + g_{i_3i_6}(\boldsymbol{x}_p)\boldsymbol{E}_{i_3i_6}], \qquad (2.44)
\end{aligned}$$

https://doi.org/10.1017/S0022377821000702 Published online by Cambridge University Press

where the discrete electric field defined on edge $i_1 i_2$ is

$$\boldsymbol{E}_{i_1 i_2} = \phi_{i_2} - \phi_{i_1}, \tag{2.45}$$

and $\boldsymbol{E}_{i_2 i_3}, \boldsymbol{E}_{i_3 i_1}, \boldsymbol{E}_{i_4 i_5}, \boldsymbol{E}_{i_5 i_6}, \boldsymbol{E}_{i_6 i_4}, \boldsymbol{E}_{i_1 i_4}, \boldsymbol{E}_{i_2 i_5}$ and $\boldsymbol{E}_{i_3 i_6}$ are defined in a similar way. The interpolation from discrete electric field to particle is defined as

$$g_{i_1 i_2} = f_{\Delta_1}(z)[f_{\Delta_1,i_2}(x,y)\nabla_\perp f_{\Delta_1,i_1}(x,y) - f_{\Delta_1,i_1}(x,y)\nabla_\perp f_{\Delta_1,i_2}(x,y)], \tag{2.46}$$

$$g_{i_2 i_3} = f_{\Delta_1}(z)[f_{\Delta_1,i_3}(x,y)\nabla_\perp f_{\Delta_1,i_2}(x,y) - f_{\Delta_1,i_2}(x,y)\nabla_\perp f_{\Delta_1,i_3}(x,y)], \tag{2.47}$$

$$g_{i_3 i_1} = f_{\Delta_1}(z)[f_{\Delta_1,i_1}(x,y)\nabla_\perp f_{\Delta_1,i_3}(x,y) - f_{\Delta_1,i_3}(x,y)\nabla_\perp f_{\Delta_1,i_1}(x,y)], \tag{2.48}$$

$$g_{i_4 i_5} = f_{\Delta_2}(z)[f_{\Delta_2,i_5}(x,y)\nabla_\perp f_{\Delta_2,i_4}(x,y) - f_{\Delta_2,i_4}(x,y)\nabla_\perp f_{\Delta_2,i_5}(x,y)], \tag{2.49}$$

$$g_{i_5 i_6} = f_{\Delta_2}(z)[f_{\Delta_2,i_6}(x,y)\nabla_\perp f_{\Delta_2,i_5}(x,y) - f_{\Delta_2,i_5}(x,y)\nabla_\perp f_{\Delta_2,i_6}(x,y)], \tag{2.50}$$

$$g_{i_6 i_4} = f_{\Delta_2}(z)[f_{\Delta_2,i_4}(x,y)\nabla_\perp f_{\Delta_2,i_6}(x,y) - f_{\Delta_2,i_6}(x,y)\nabla_\perp f_{\Delta_2,i_4}(x,y)], \tag{2.51}$$

and

$$g_{i_1 i_4} = f_{\Delta_1,i_1}(x,y)\left[f_{\Delta_2}(z)\frac{\partial}{\partial z}f_{\Delta_1}(z) - f_{\Delta_1}(z)\frac{\partial}{\partial z}f_{\Delta_2}(z)\right], \tag{2.52}$$

$$g_{i_2 i_5} = f_{\Delta_1,i_2}(x,y)\left[f_{\Delta_2}(z)\frac{\partial}{\partial z}f_{\Delta_1}(z) - f_{\Delta_1}(z)\frac{\partial}{\partial z}f_{\Delta_2}(z)\right], \tag{2.53}$$

$$g_{i_3 i_6} = f_{\Delta_1,i_3}(x,y)\left[f_{\Delta_2}(z)\frac{\partial}{\partial z}f_{\Delta_1}(z) - f_{\Delta_1}(z)\frac{\partial}{\partial z}f_{\Delta_2}(z)\right]. \tag{2.54}$$

The diagram of the algorithm is shown in figure 3. The charge-deposition algorithm is shown in figure 3(*a*). Figure 3(*b*) shows the electric field on each edge calculated as (2.45). The electric field is interpolated to a particle's position by (2.46)–(2.54) as shown in figure 3(*c*). Note that (2.46)–(2.54) are consistent with the formalism of Whitney 1-forms on a prism mesh (Nedelec 1980; Lohi & Kettunen 2021). In the PIC code, we take the linear barycentric function for $f_{\Delta_1,i_1}(x,y)$, $f_{\Delta_1,i_2}(x,y)$ and $f_{\Delta_1,i_3}(x,y)$, and we take the tent function for $f_{\Delta_1}(z)$ and $f_{\Delta_2}(z)$.

3. Ion Bernstein waves on 2-D unstructured meshes

The PIC method described in § 2 is used to examine the IBW (Bernstein 1958) in 2-D uniform plasmas. The simulations are carried out in a rectangular region with periodic boundary conditions and in a 2-D circular region with fixed boundary conditions.

3.1. *The IBW with periodic boundary conditions in a rectangular region*

First, the IBW in a rectangular region of a uniform plasma is examined on an unstructured mesh with periodic boundary conditions. The simulation domain is shown in figure 4(*a*), and figure 4(*b*) shows a zoom-in of the red region. The simulation domain has 20 201 vertices and 40 000 triangles. To implement the periodic boundary conditions, each vertex at the left-hand boundary is identified with the corresponding vertex at the right-hand boundary. Similar identification is imposed for the top and bottom boundaries. The ion mass is $m_i = 1.67 \times 10^{-27}$ kg and charge is $q_i = 1.6 \times 10^{-19}$ C, the initial ion density is $n_{i0} = 10^{20}$ m^{-3}, the electron and ion temperatures are 1000 eV and the out-of-plane background magnetic field is $B_0 = 2$ T. The simulation time step is $\Delta t = 0.01/\Omega_i$ and the total number of simulation particles is 5.12×10^7.

https://doi.org/10.1017/S0022377821000702 Published online by Cambridge University Press

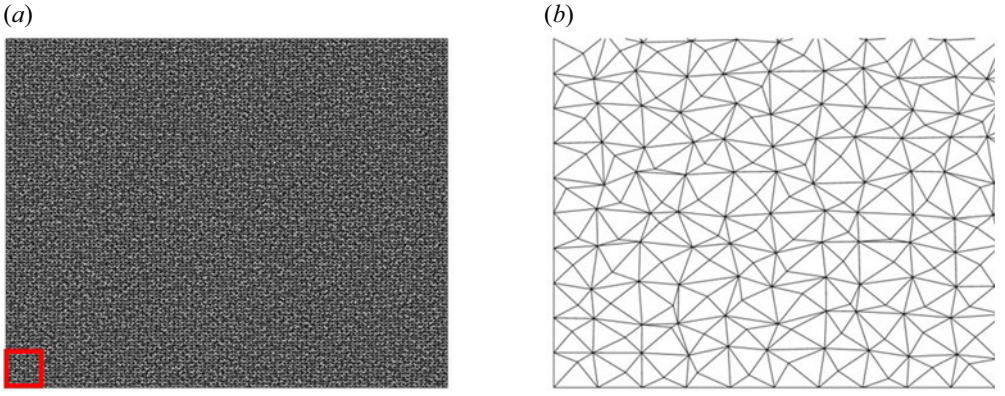

FIGURE 4. (*a*) The rectangular simulation domain. (*b*) A zoom-in of the red rectangular region in (*a*).

During the simulation, the electric potential ϕ on each vertex is recorded. The potentials ϕ on the vertices are interpolated to a rectangular mesh; after interpolation, data are analysed using the fast Fourier transform. The dispersion relations of the IBW can be inferred from $\tilde{\phi}(k_x, k_y, \omega)$, where k_x and k_y are the wave numbers in the x and y directions and ω is the angular frequency. Figure 5 plots the contours of the spectral power of $\tilde{\phi}$, and the contour peaks show the dispersion relation k_x–ω at a fixed k_y, where k_x and k_y are normalized to the ion gyroradius ρ_i and ω to the ion gyrofrequency Ω_i. The contour plots of $\tilde{\phi}$ at $k_y\rho_i = 0$, 1.0, 2.0 and 3.0 are shown in figure 5. The contour plots are compared with the theoretical dispersion relation with kinetic ions and adiabatic electrons (Sturdevant 2016):

$$1 + \theta \sum_{n=-\infty}^{\infty} \frac{n\Omega_i \Gamma_n(b)}{\omega + n\Omega_i} = 0. \tag{3.1}$$

Here, $\theta = q_i T_e / q_e T_i$, $b \equiv (k_\perp \rho_i)^2$, $\Gamma_n \equiv I_n(b) e^{-b}$, $k_\perp$ is the perpendicular wave number and I_n is the nth modified Bessel function of the first kind. For the present 2-D simulation, $k_\perp = \sqrt{k_x^2 + k_y^2}$. The dispersion relation in terms of (k_x, k_y, ω) can be directly compared with the dispersion relation from the PIC simulation. The red dashed lines in figure 5 are the dispersion relation curves at $k_y\rho_i = 0$, 1.0, 2.0, 3.0 from (3.1). The dispersion relations from the PIC simulations agree well with the theory. We also carry out the simulations on prism and tetrahedral meshes and obtain the dispersion relations of IBW for $k_{||} = 0$; the dispersion relations are consistent with the theory results.

3.2. *The IBW in a 2-D circular region with fixed boundary conditions*

In this subsection, we simulate the IBW in a 2-D circular domain using an unstructured mesh. The simulation domain is shown in figure 6(*a*), and figure 6(*b*) shows a zoom-in of the red rectangular region. The simulation domain has 7477 vertices and 14 646 triangles. The physical parameters are the same as in § 3.1. The total number of simulation particles is 4.9×10^{10} in order to reduce noise and obtain eigenmode structures by the nonlinear PIC simulation, and the time step is $\Delta t = 0.02/\Omega_i$. The boundary condition is that $\phi = 0$ at the outermost vertices, and particles are reflected when entering the outermost triangles.

For the fast Fourier transform analysis, ϕ is interpolated to a diagnostic circular mesh which has 101 co-concentric circles with equal intervals, and 61 grid points are distributed

https://doi.org/10.1017/S0022377821000702 Published online by Cambridge University Press

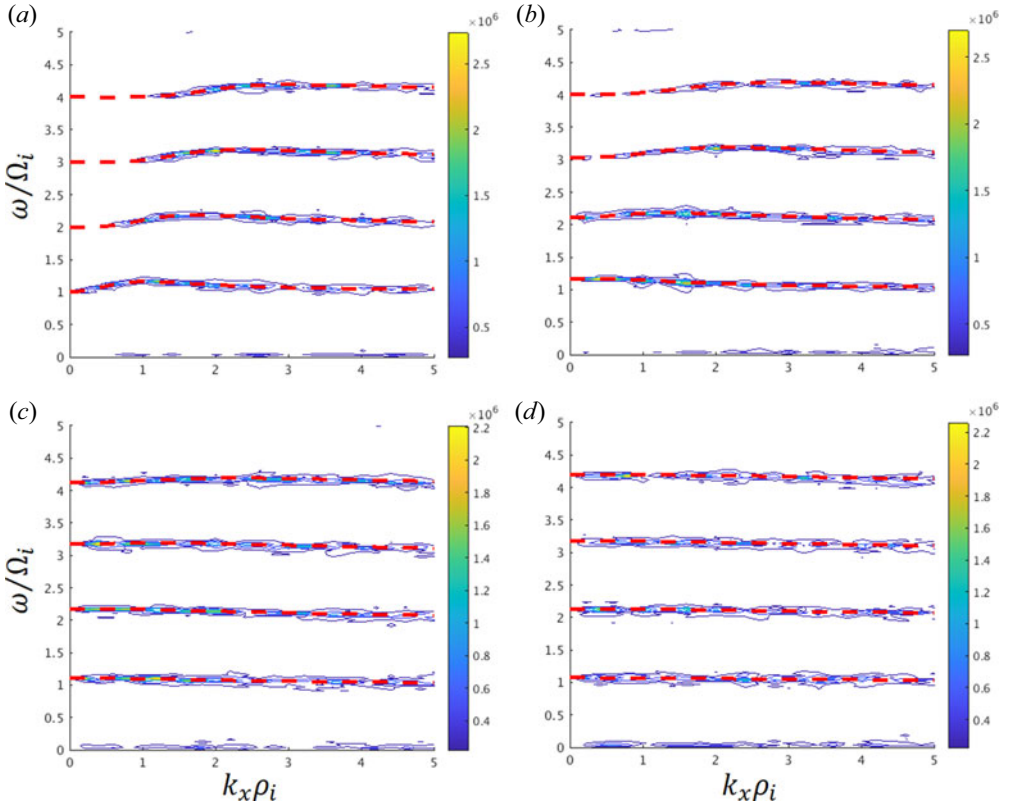

FIGURE 5. Dispersion relation of the IBW in a 2-D rectangular domain. The contour plot of $\tilde{\phi}(k_x, \omega)$ at (*a*) $k_y\rho_i = 0$, (*b*) $k_y\rho_i = 1.0$, (*c*) $k_y\rho_i = 2.0$ and (*d*) $k_y\rho_i = 3.0$. The red dashed lines represent the theoretical dispersion relation.

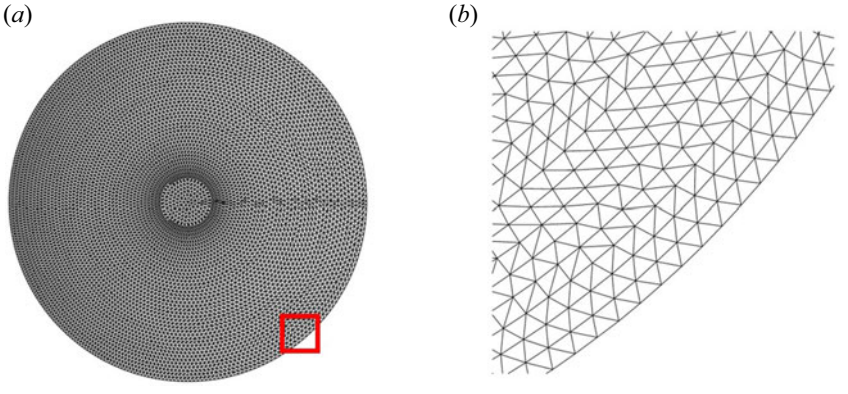

FIGURE 6. (*a*) The 2-D circular simulation domain. (*b*) A zoom-in of the red rectangular region in (*a*).

https://doi.org/10.1017/S0022377821000702 Published online by Cambridge University Press

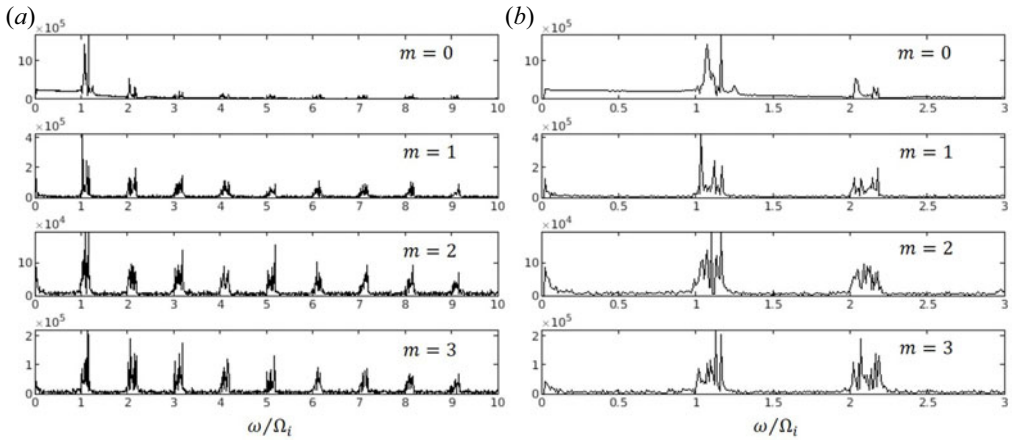

FIGURE 7. (*a*) Spectrum of the IBW for $m = 0, 1, 2, 3$. (*b*) Zoom-in of (*a*) for $0 \leq \omega/\Omega_i \leq 3$.

on each circle with the same angular interval. On the diagnostic mesh, ϕ is a function of time t and the radial coordinates (r, θ). Performing the fast Fourier transform analysis of $\phi(r, \theta, t)$ along the θ and t directions, we discover that for each azimuthal mode number m, the spectrum of the system has a rich structure that can be labelled by two integer indices, n and l. In the neighbourhood of each integer harmonics of Ω_i labelled by n, there exists a family of eigenmodes labelled by l. The value of l indicates the number of oscillations of the eigenmode in the radial direction. Thus, the eigenmode expansion for ϕ is

$$\phi = \sum_{n,m,l} \tilde{\phi}_{nml}(r) \exp(im\theta - i\omega_{nml}t), \tag{3.2}$$

where $\tilde{\phi}_{nml}(r)$ is the eigenfunction of the mode at $\omega = \omega_{nml}$. Figure 7(*a*) plots the spectrum of $\tilde{\phi}$ for $m = 0, 1, 2, 3$, where the frequency ω is normalized to ion gyrofrequency Ω_i. Figure 7(*b*) shows a zoom-in of the spectrum in the range $0 \leq \omega/\Omega_i \leq 3$. The eigenmode structures $\tilde{\phi}_{nml}(r)$ for $m = 0, 1, 2, 3$, $l = 1, 2, 3$ in the neighbourhood of the first harmonic ($n = 1$) are shown in figure 8. We are not aware of any previous study of these eigenmodes of the IBW in a circular domain.

4. Comparison of PIC methods on unstructured meshes

As discussed in § 1, previous PIC methods on unstructured meshes used identical shape function for both charge deposition and field interpolation (Celik *et al.* 2003; Spirkin & Gatsonis 2004). In this section, the energy conservation property of our PIC method (Method A) is compared with that of a PIC method (Method B) using identical shape function for both charge deposition and field interpolation. The comparison is carried out on an unstructured mesh as in figure 4.

Method B on the unstructured mesh is illustrated in figure 9. Suppose a particle at (x, y) is inside a triangle. The charge of the particle is deposited to the triangular vertices by the linear barycentric functions, as shown in figure 9(*a*). The electric potential ϕ_I is calculated from ρ_I by (2.12). With the ϕ_I on each vertex, the electric field components E_x and E_y are calculated by a centred finite-difference method (Birdsall & Langdon 1991). At (x_{i_1}, y_{i_1}), the x component of the electric field is

$$E_x = \frac{\phi(x_{i_1} + \Delta x, y_{i_1}) - \phi(x_{i_1} - \Delta x, y_{i_1})}{2\Delta x}, \tag{4.1}$$

https://doi.org/10.1017/S0022377821000702 Published online by Cambridge University Press

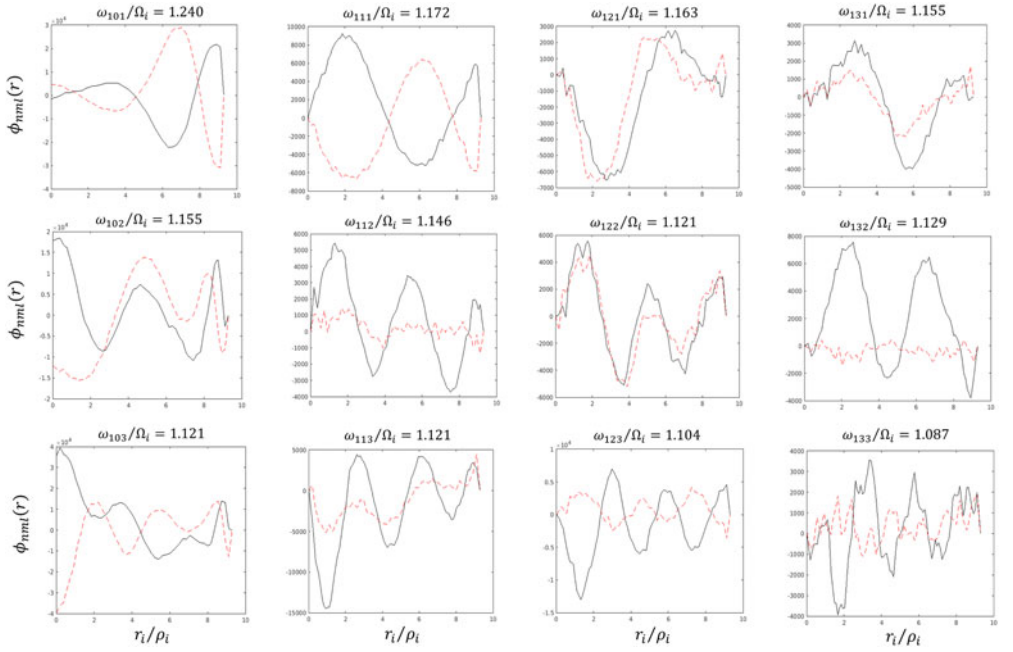

FIGURE 8. Eigenmode structures $\tilde{\phi}_{nml}(r)$ for $m = 0, 1, 2, 3$ and $l = 1, 2, 3$ in the neighbourhood of the first harmonic ($n = 1$). The black solid line is the real part of $\tilde{\phi}_{nml}(r)$ and the red dashed line is the imaginary part. The eigenfrequency ω_{nml} for each eigenmode is listed.

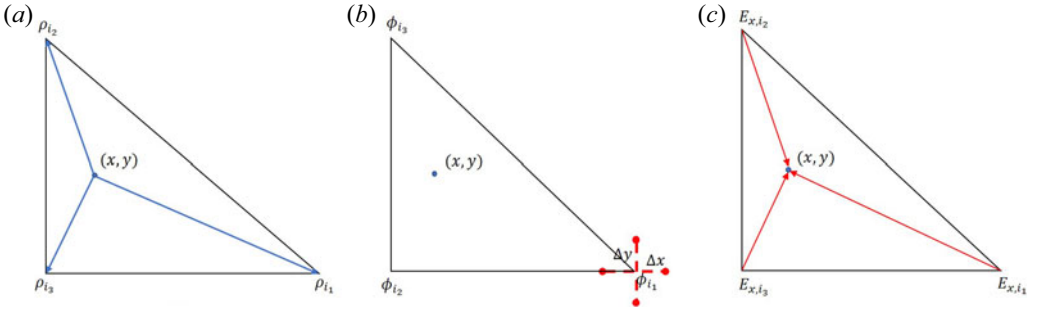

FIGURE 9. A previous PIC method (Method B) on unstructured meshes with identical shape function for charge deposition and field interpolation. (*a*) Depositing the particle's charge into the triangular vertices. (*b*) Computing E_x and E_y by a five-point finite-difference method. (*c*) Interpolating $\boldsymbol{E}$ from vertices to the particle's position.

where $\Delta x, \Delta y$ is chosen to be a small value compared with the averaged length of triangular edges. To calculate $\phi(x_{i_1} \pm \Delta x, y_{i_1})$, we first determine the triangle in which the point $(x_{i_1} \pm \Delta x, y_{i_1})$ locates, and then interpolate ϕ at $(x_{i_1} \pm \Delta x, y_{i_1})$ from its values on the triangular vertices using linear barycentric functions, as shown in figure 9(*b*). Component E_y can be calculated using a similar method. As figure 9(*c*) shows, to advance the particle's position and velocity, $\boldsymbol{E}$ at the particle's position (x, y) is obtained by interpolating $\boldsymbol{E}$ at the triangular vertices to (x, y) using the linear barycentric function. Note that Method B uses the linear barycentric functions for both charge deposition and field interpolation.

Contrast simulations of Methods A and B are carried out on the unstructured mesh with periodic boundary conditions. The horizontal length of the mesh is 10 times larger than

https://doi.org/10.1017/S0022377821000702 Published online by Cambridge University Press

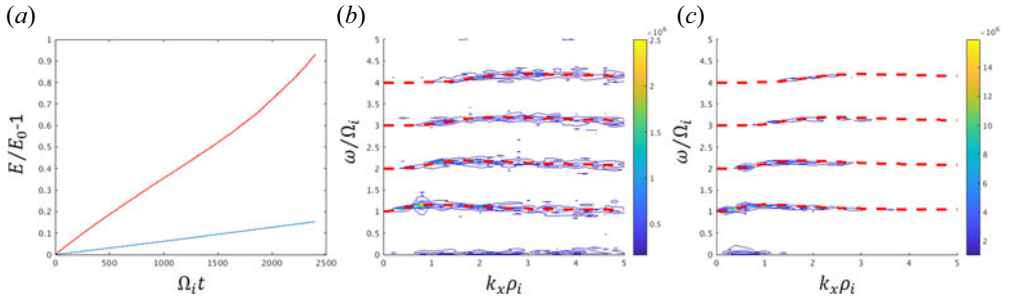

FIGURE 10. Comparison between our algorithm derived from the discrete variational principle (Method A) and a previous method using identical shape function for charge deposition and field interpolation (Method B). (*a*) The total energy error during the simulation. The blue curve is for method A and the red curve is for Method B. (*b*) The dispersion relation obtained from Method A. The red dashed lines are the theoretical results. (*c*) The dispersion relation obtained from Method B.

the vertical length. The mesh has 2111 vertices and 4000 triangles. For Method B, Δx is chosen to be 1/10 of averaged length of triangular edges. The physical parameters are the same as in § 3.1. For both simulations, the time step is $\Delta t = 0.02/\Omega_i$ and the number of simulation particles is 1.28×10^6. Both simulations are performed to the time length of $2400/\Omega_i$.

Figure 10(*a*) shows a comparison of the energy conservation property of Methods A and B. We measure the error of total energy during the simulations. Here E is the total energy that includes plasma kinetic energy, particles' potential energy and electric field energy, and E_0 is the initial total energy. The blue line is the total energy error of Method A and the red line is that of Method B. The growth rate of total energy error of Method B is six times faster than that of Method A. The IBW dispersion relation for $k_y = 0$ at $t \sim 1800/\Omega_i$ is shown in figures 10(*b*) and 10(*c*) for Method A and Method B, respectively. The dispersion relation from Method A agrees wells with the theoretical results. In contrast, the contour plot from Method B cannot recover the dispersion relation for all harmonics in the regime of $k_x\rho_i \geq 3$. Method A has a much smaller total energy error, and thus generates a more accurate dispersion relation. This comparison study demonstrates that our new algorithm derived from the discrete variational principle has a much better energy conservation property than previous methods using identical shape function for charge deposition and field interpolation. We point out that many PIC methods adopt identical shape function for both charge deposition and field interpolation in order to conserve momentum. These PIC methods are commonly referred to as 'momentum conserving' methods. However, as Hockney & Eastwood (1981) and Birdsall & Langdon (1991) stated, besides using identical shape function for both charge deposition and field interpolation, a PIC method must have 'correctly space-centred difference approximation to derivatives' (Hockney & Eastwood 1981) or 'left–right symmetry' (Birdsall & Langdon 1991) to have momentum conservation. Solely adopting identical shape function for both charge deposition and field interpolation, as in Method B and previous PIC methods (Celik *et al.* 2003; Spirkin & Gatsonis 2004; Gatsonis & Spirkin 2009; Day 2011; Han *et al.* 2016), cannot guarantee momentum conservation on an unstructured mesh. In addition, under the assumption of electron adiabatic response, the high-frequency electron motion does not affect IBWs. The geometric PIC algorithm can have a speed-up by a factor of 10^4 with similar accuracy for studying IBWs comparing with standard PIC algorithms which compute the high-frequency motion of six-dimensional electrons.

https://doi.org/10.1017/S0022377821000702 Published online by Cambridge University Press

5. Conclusions and discussion

In conclusion, we have built a geometric electrostatic PIC method on unstructured triangular, tetrahedral and prism meshes. The PIC method uses kinetic ions and adiabatic electrons. The discrete variational principle gives an algorithm that deposits particle charge to triangular vertices by Whitney 0-forms and interpolates the electric field at particle positions using the values on the triangular edges and Whitney 1-forms. The formula of Whitney forms, the discrete exterior calculus method that computes the discrete electric field on triangular edges and the algorithm of charge deposition and field interpolation are described in detail. The PIC method has been used to investigate IBWs on unstructured meshes with two different geometries and boundary conditions. For the case with periodic boundary conditions in a rectangular domain, the simulated dispersion relation agrees well with the theory. For the case on a 2-D circular unstructured mesh with fixed boundary conditions, the spectrum and eigenmode structures are obtained. The simulation results of our PIC algorithm are compared with those of a previous PIC method using identical shape function for charge deposition and field interpolation. The comparison shows the new algorithm has a much better energy conservation property and thus can give a more accurate dispersion relation. Higher-order Whitney forms can significantly reduce the noise and improve the energy conservation property of a PIC algorithm. In a cubic mesh, Xiao *et al.* (2015*b*, 2016) constructed high-order Whitney forms spanning over multiple cells with chosen functions for the Whitney 0-forms. The high-order Whitney forms have significantly reduced the noise and improved the energy conservation property of the PIC simulations. Rapetti & Bossavit (2009) proposed another type of high-order Whitney forms on triangular and tetrahedral meshes. Midpoints on edges are introduced to split a triangle into a set of subtriangles, and Whitney 0-forms and Whitney 1-forms are built using the subtriangles. These high-order Whitney forms can improve the accuracy of solving partial differential equations. However, our numerical test shows that when implemented in the PIC algorithm, this type of high-order Whitney forms introduces larger energy error. This implies that we should design high-order Whitney forms for PIC algorithms from the discrete variational principle, instead of adopting those used for partial differential equation algorithms. The present paper focuses on demonstrating the new charge-deposition and field-interpolation methods on unstructured meshes and has not implemented the symplectic structure-preserving integration algorithm. The topic of symplectic structure-preserving integration on unstructured meshes will be addressed in future studies.

Acknowledgements

The computing resources were provided on the PPPL computer Traverse operated by the Princeton Institute for Computational Science and Engineering (PICSciE) and Cori at NERSC, a US Department of Energy Office of Science User Facility located at Lawrence Berkeley National Laboratory, operated under contract no. DE-AC02-05CH11231.

Editor Luís O. Silva thanks the referees for their advice in evaluating this article.

Funding

This research was supported by the US Department of Energy Office of Science ASCR and FES through SciDAC-4 Partnership Center for High-fidelity Boundary Plasma Simulation (HBPS), under contract no. DE-AC02-09CH11466 through Princeton University.

Declaration of interest

The authors report no conflict of interest.

REFERENCES

BERNSTEIN, I.B. 1958 Waves in a plasma in a magnetic field. *Phys. Rev*. **109** (1), 10–21.

BIRDSALL, C. & LANGDON, A.B. 1991 *Plasma Physics via Computer Simulation*. Adam Hilger.

BORIS, J. 1970 In *Proceedings of the Fourth Conference on Numerical Simulation of Plasmas*, p. 3. Naval Research Laboratory.

BOSSAVIT, A. 1988 Whitney forms: a class of finite elements for three-dimensional computations in electromagnetism. *IEE Proc. Phys. Sci. Meas. Instrum. Manage. Educ. Rev*. **135** (8), 493.

BOSSAVIT, A. 1998 *Computational Electromagnetism: Variational Formulations, Complementarity, Edge Elements*. Academic Press.

BURBY, J.W. 2017 Finite-dimensional collisionless kinetic theory. *Phys. Plasmas* **24** (3), 032101.

CELIK, M., SANTI, M., CHENG, S., MARTÍNEZ-SÁNCHEZ, M. & PERAIRE, J. 2003 Hybrid-pic simulation of hall thrusterplume on an unstructured grid with dsmc collisions. In *28th International Electric Propulsion. Conference, Toulouse, March 2003*.

CHANG, C.S., KU, S., DIAMOND, P.H., LIN, Z., PARKER, S., HAHM, T.S. & SAMATOVA, N. 2009 Compressed ion temperature gradient turbulence in diverted tokamak edge. *Phys. Plasmas* **16** (5), 056108.

CHANG, C.S., KU, S., TYNAN, G.R., HAGER, R., CHURCHILL, R.M., CZIEGLER, I., GREENWALD, M., HUBBARD, A.E. & HUGHES, J.W. 2017 Fast low-to-high confinement mode bifurcation dynamics in a tokamak edge plasma gyrokinetic simulation. *Phys. Rev. Lett*. **118** (17).

CHANG, C.S., KU, S. & WEITZNER, H. 2004 Numerical study of neoclassical plasma pedestal in a tokamak geometry. *Phys. Plasmas* **11** (5), 2649–2667.

DAWSON, J.M. 1983 Particle simulation of plasmas. *Rev. Mod. Phys*. **55** (2), 403–447.

DAWSON, J.M., OKUDA, H. & ROSEN, B. 1976 Collective transport in plasmas. In *Methods in Computational Physics: Advances in Research and Applications*, pp. 281–325. Elsevier.

DAY, D.M. 2011 Numerical experiments on unstructured pic stability. *Tech. Rep.* Sandia National Laboratories.

DESBRUN, M., KANSO, E. & TONG, Y. 2008 Discrete differential forms for computational modeling. In *Discrete Differential Geometry*, pp. 287–324. Birkhäuser.

ELLISON, C.L., BURBY, J.W. & QIN, H. 2015 Comment on "symplectic integration of magnetic systems": a proof that the boris algorithm is not variational. *J. Comput. Phys*. **301**, 489–493.

GATSONIS, N.A. & SPIRKIN, A. 2009 A three-dimensional electrostatic particle-in-cell methodology on unstructured Delaunay–Voronoi grids. *J. Comput. Phys*. **228** (10), 3742–3761.

GLASSER, A.S. & QIN, H. 2020 The geometric theory of charge conservation in particle-in-cell simulations. *J. Plasma Phys*. **86** (3), 835860303.

HAN, D., WANG, P., HE, X., LIN, T. & WANG, J. 2016 A 3d immersed finite element method with non-homogeneous interface flux jump for applications in particle-in-cell simulations of Plasma–Lunar surface interactions. *J. Comput. Phys*. **321**, 965–980.

HE, Y., QIN, H., SUN, Y., XIAO, J., ZHANG, R. & LIU, J. 2015*a* Hamiltonian time integrators for Vlasov-Maxwell equations. *Phys. Plasmas* **22** (12), 124503.

HE, Y., SUN, Y., LIU, J. & QIN, H. 2015*b* Volume-preserving algorithms for charged particle dynamics. *J. Comput. Phys*. **281**, 135–147.

HE, Y., SUN, Y., LIU, J. & QIN, H. 2016*a* Higher order volume-preserving schemes for charged particle dynamics. *J. Comput. Phys*. **305**, 172–184.

HE, Y., SUN, Y., QIN, H. & LIU, J. 2016*b* Hamiltonian particle-in-cell methods for Vlasov-Maxwell equations. *Phys. Plasmas* **23** (9), 092108.

HE, Y., SUN, Y., ZHANG, R., WANG, Y., LIU, J. & QIN, H. 2016*c* High order volume-preserving algorithms for relativistic charged particles in general electromagnetic fields. *Phys. Plasmas* **23** (9), 092109.

HE, Y., ZHOU, Z., SUN, Y., LIU, J. & QIN, H. 2017 Explicit k-symplectic algorithms for charged particle dynamics. *Phys. Lett.* A **381** (6), 568–573.

HIRANI, A.N. 2003 Discrete exterior calculus. PhD thesis, California Institute of Technology.

HOCKNEY, R. & EASTWOOD, J.W. 1981 *Computer Simulation using Particles*. McGraw-Hill International Book Co.

HORTON, W. 1999 Drift waves and transport. *Rev. Mod. Phys*. **71** (3), 735–778.

HU, Y., MIECNIKOWSKI, M., CHEN, Y. & PARKER, S. 2018 Fully kinetic simulation of ion-temperature-gradient instabilities in tokamaks. *Plasma* **1** (1), 105–118.

KORMANN, K. & SONNENDRÜCKER, E. 2021 Energy-conserving time propagation for a structure-preserving particle-in-cell Vlasov–Maxwell solver. *J. Comput. Phys*. **425**, 109890.

KRAUS, M., KORMANN, K., MORRISON, P.J. & SONNENDRÜCKER, E. 2017 GEMPIC: geometric electromagnetic particle-in-cell methods. *J. Plasma Phys*. **83** (4), 905830401.

KU, S., CHANG, C.-S., ADAMS, M., CUMMINGS, J., HINTON, F., KEYES, D., KLASKY, S., LEE, W., LIN, Z., PARKER, S. & THE CPES TEAM 2006 Gyrokinetic particle simulation of neoclassical transport in the pedestal/scrape-off region of a tokamak plasma. *J. Phys.: Conf. Ser*. **46**, 87–91.

KU, S., CHANG, C.S., HAGER, R., CHURCHILL, R.M., TYNAN, G.R., CZIEGLER, I., GREENWALD, M., HUGHES, J., PARKER, S.E., ADAMS, M.F., D'AZEVEDO, E. & WORLEY, P. 2018 A fast low-to-high confinement mode bifurcation dynamics in the boundary-plasma gyrokinetic code XGC1. *Phys. Plasmas* **25** (5), 056107.

LANGDON, A.B. 1970 Effects of the spatial grid in simulation plasmas. *J. Comput. Phys*. **6** (2), 247–267.

LEE, T.D. 1983 Can time be a discrete dynamical variable? *Phys. Lett.* B **122** (3-4), 217–220.

LI, Y., HE, Y., SUN, Y., NIESEN, J., QIN, H. & LIU, J. 2019 Solving the Vlasov–Maxwell equations using Hamiltonian splitting. *J. Comput. Phys*. **396**, 381–399.

LOHI, J. & KETTUNEN, L. 2021 Whitney forms and their extensions. *J. Comput. Appl. Math*. **393**, 113520.

MARSDEN, J.E. & WEST, M. 2001 Discrete mechanics and variational integrators. *Acta Numer*. **10**, 357–514.

MIECNIKOWSKI, M.T., STURDEVANT, B.J., CHEN, Y. & PARKER, S.E. 2018 Nonlinear saturation of the slab ITG instability and zonal flow generation with fully kinetic ions. *Phys. Plasmas* **25** (5), 055901.

MOON, H., TEIXEIRA, F.L. & OMELCHENKO, Y.A. 2015 Exact charge-conserving Scatter–Gather algorithm for particle-in-cell simulations on unstructured grids: a geometric perspective. *Comput. Phys. Commun*. **194**, 43–53.

MORRISON, P.J. 2017 Structure and structure-preserving algorithms for plasma physics. *Phys. Plasmas* **24** (5), 055502.

NEDELEC, J.C. 1980 Mixed finite elements in r^3. *Numer. Math*. **35** (3), 315–341.

PERSE, B., KORMANN, K. & SONNENDRÜCKER, E. 2021 Geometric particle-in-cell simulations of the Vlasov–Maxwell system in curvilinear coordinates. *SIAM J. Sci. Comput*. **43** (1), B194–B218.

POTTER, D. 1973 *Computational Physics*. John Weily.

QIN, H. 2020 Machine learning and serving of discrete field theories. *Sci. Rep*. **10**, 19329.

QIN, H. & GUAN, X. 2008 Variational symplectic integrator for long-time simulations of the guiding-center motion of charged particles in general magnetic fields. *Phys. Rev. Lett*. **100**, 035006.

QIN, H., GUAN, X. & TANG, W.M. 2009 Variational symplectic algorithm for guiding center dynamics and its application in tokamak geometry. *Phys. Plasmas* **16** (4), 042510.

QIN, H., LIU, J., XIAO, J., ZHANG, R., HE, Y., WANG, Y., SUN, Y., BURBY, J.W., ELLISON, L. & ZHOU, Y. 2016 Canonical symplectic particle-in-cell method for long-term large-scale simulations of the Vlasov–Maxwell equations. *Nucl. Fusion* **56** (1), 014001.

QIN, H., ZHANG, S., XIAO, J., LIU, J., SUN, Y. & TANG, W.M. 2013 Why is boris algorithm so good? *Phys. Plasmas* **20** (8), 084503.

RAPETTI, F. & BOSSAVIT, A. 2009 Whitney forms of higher degree. *SIAM J. Numer. Anal*. **47** (3), 2369–2386.

SPIRKIN, A. & GATSONIS, N.A. 2004 Unstructured 3d PIC simulations of the flow in a retarding potential analyzer. *Comput. Phys. Commun*. **164** (1-3), 383–389.

SQUIRE, J., QIN, H. & TANG, W.M. 2012*a* Geometric integration of the vlasov-maxwell system with a variational particle-in-cell scheme. *Phys. Plasmas* **19** (8), 084501.

SQUIRE, J., QIN, H. & TANG, W.M. 2012*b* Geometric integration of the Vlasov-Maxwell system with a variational particle-in-cell scheme. *Tech. Rep.* PPPL-4748. Princeton Plasma Physics Laboratory.

STURDEVANT, B. 2016 Fully kinetic ion models for magnetized plasma simulations. PhD thesis, University of Colorado.

STURDEVANT, B.J., CHEN, Y. & PARKER, S.E. 2017 Low frequency fully kinetic simulation of the toroidal ion temperature gradient instability. *Phys. Plasmas* **24** (8), 081207.

VESELOV, A.P. 1988 Integrable discrete-time systems and difference operators. *Funct. Anal. Appl*. **22** (2), 83–93.

WEILAND, J. 2012 *Stability and Transport in Magnetic Confinement Systems*. Springer.

WHITNEY, H. 1957 *Geometric Integration Theory*. Princeton University Press.

XIAO, J., LIU, J., QIN, H. & YU, Z. 2013 A variational multi-symplectic particle-in-cell algorithm with smoothing functions for the Vlasov-Maxwell system. *Phys. Plasmas* **20** (10), 102517.

XIAO, J., LIU, J., QIN, H., YU, Z. & XIANG, N. 2015*a* Variational symplectic particle-in-cell simulation of nonlinear mode conversion from extraordinary waves to Bernstein waves. *Phys. Plasmas* **22** (9), 092305.

XIAO, J. & QIN, H. 2019 Field theory and a structure-preserving geometric particle-in-cell algorithm for drift wave instability and turbulence. *Nucl. Fusion* **59** (10), 106044.

XIAO, J. & QIN, H. 2021 Explicit structure-preserving geometric particle-in-cell algorithm in curvilinear orthogonal coordinate systems and its applications to whole-device 6d kinetic simulations of tokamak physics. *Plasma Sci. Technol*. **23** (5), 055102.

XIAO, J., QIN, H. & LIU, J. 2018 Structure-preserving geometric particle-in-cell methods for Vlasov-Maxwell systems. *Plasma Sci. Technol*. **20** (11), 110501.

XIAO, J., QIN, H., LIU, J., HE, Y., ZHANG, R. & SUN, Y. 2015*b* Explicit high-order non-canonical symplectic particle-in-cell algorithms for Vlasov-Maxwell systems. *Phys. Plasmas* **22** (11), 112504.

XIAO, J., QIN, H., LIU, J. & ZHANG, R. 2017 Local energy conservation law for a spatially-discretized Hamiltonian Vlasov-Maxwell system. *Phys. Plasmas* **24** (6), 062112.

XIAO, J., QIN, H., MORRISON, P.J., LIU, J., YU, Z., ZHANG, R. & HE, Y. 2016 Explicit high-order noncanonical symplectic algorithms for ideal two-fluid systems. *Phys. Plasmas* **23** (11), 112107.

ZHANG, R., LIU, J., QIN, H., WANG, Y., HE, Y. & SUN, Y. 2015 Volume-preserving algorithm for secular relativistic dynamics of charged particles. *Phys. Plasmas* **22** (4), 044501.

ZHENG, J., CHEN, J., LU, F., XIAO, J., AN, H. & SHEN, L. 2020 Structure-preserving electromagnetic–kinetic simulations of lower hybrid-wave injection and current drive. *Plasma Phys. Control. Fusion* **62** (12), 125020.